Journal of Quantitative Spectroscopy & Radiative Transfer 113 (2012) 1762–1770

Contents lists available at SciVerse ScienceDirect

Journal of Quantitative Spectroscopy & Radiative Transfer

journal homepage: www.elsevier.com/locate/jqsrt

Photoionization and electron–ion recombination of Fe XVII for high temperature plasmas

Sultana N. Nahar*

Department of Astronomy, The Ohio State University, Columbus, OH 43210, USA

ARTICLE INFO

Article history:
Received 13 January 2012
Received in revised form
2 May 2012
Accepted 3 May 2012
Available online 11 May 2012

Keywords:
Photoionization and electron–ion recombination
Fe XVII
Solar plasma

ABSTRACT

Earlier studies on electron–ion recombination of Fe XVII, $e+\text{Fe XVIII}\rightarrow\text{Fe XVII}$, concentrated on low temperature region. However, due to its higher abundance, recombination in the high temperature region is of great importance. Total and level-specific recombination cross sections and rates of Fe XVII are presented from the detailed study in the high temperature. The calculations were carried out using the unified method which incorporates both the radiative recombination (RR) and dielectronic recombination (DR) including the interference effects. The method also yields self-consistent set of recombination rates and photoionization cross sections. Unified method is implemented through relativistic Breit–Pauli R-matrix (BPRM) method and close coupling (CC) approximation. For the details of the high energy and high temperature features a CC wave function expansion consisting of 60 levels from $n=2$ and 3 complexes of the core Fe XVIII was considered. Earlier study included core excitations to $n=2$ levels only. It is found that the resonances due to core excitations to $n=3$ levels are much more extensive and stronger than those to $n=2$ levels and increase the recombination considerably in the high temperature region. While earlier study of 3-level calculations agree very well with the experimentally derived low temperature recombination, the high temperature rate shows a broad peak at about 5×10^6 K, near the maximum abundance of the ion, due to dominance of DR via PEC (photo-excitation-of-core) resonances of $n=3$ levels. Level-specific recombination rate coefficients, which include both the RR and DR, are presented for 454 levels ($n\leq10$, $l\leq9$, $0\leq J\leq8$ with even and odd parities) of Fe XVII. This is the first large-scale BPRM calculations for recombination of a complex atomic system beyond He- and Li-like ions. The results are expected to be accurate with 10–20% uncertainty and provide accurate modelings of ultraviolet to X-ray spectra.

1. Introduction

Fe XVII is a primary source of X-ray emission in astronomical objects. Lines of the ion have been seen in photoionized plasmas which typically are in low temperature. However, the ion is more abundant in coronal plasmas and the temperature of maximum abundance in coronal ionization equilibrium is about 4×10^6 K [1]. The ion has been detected in the warm absorber ionized gas surrounding the central black hole in active galactic nuclei (e.g. [2]). Through analysis of the emission spectra information about physical conditions and chemical compositions or reactions in the plasmas can be extracted. Photoionization and recombination cause absorption and emission lines. Due to its importance, Fe XVII has been under study by many, both theoretically (e.g. [2–7]) and experimentally [8]. However, studies on recombination remained in the low temperature region. Complete

* Tel.: +1 614 292 1888; fax: +1 614 292 2928.
E-mail address: nahar@astronomy.ohio-state.edu

0022-4073/$ - see front matter © 2012 Elsevier Ltd. All rights reserved.
http://dx.doi.org/10.1016/j.jqsrt.2012.05.003

analysis of the observed spectra requires study of processes, such as, electron-impact excitations, bound–bound transitions, photoionization, and electron–ion recombination. Results on Fe XVII using relativistic ab initio Breit–Pauli R-matrix method [9,10] on electron-impact excitations [11], oscillator strengths [12], photoionization and recombination in the low energy and temperature region [13], photoionization for a single symmetry [5] and all symmetries up to $n=10$ [14] using a large 60CC wave function expansion have already been reported.

Our reported recombination rate coefficients of Fe XVII in the low energy and temperature regions [13] showed very good agreement with experimentally rates [8]. However, for practical applications the ion needs to be studied in the high energy and temperature that require the cross sections to be calculated up to high energies in variety of conditions where L-shell ions are abundant. The present work, based on a 60 level wave function expansion enranging high energy, is involved with many infinite series of resonance converging on to the various excited levels of the core ion. Hence the relativistic BPRM calculations are much more extensive than those for He- and Li-like ions using the same method. It may be noted that BPRM method is now being used for complex systems by various authors and groups. However, they are mostly for limited number of low lying levels.

2. Theory

Photoionization and electron–ion recombination are inverse processes both of which can occur directly or through an intermediate autoionizing state. In direct photoionization an electron absorbs the incoming photon and leaves the ion and the inverse is the radiative recombination (RR)

$$e+X^{++}\leftrightarrow h\nu+X^{+}. \tag{1}$$

Direct process gives the nonresonant background cross section. However, with an intermediate quasi-bound state known as the autoionizing state, two electrons are excited which can lead either to autoionization (radiation-less transition) where the electron goes free or to dielectronic recombination (DR) where a photon is released (radiation damping) leading to capture of the outer electron

$$e+X^{++}\rightarrow(X^{+})^{**}\rightarrow\begin{cases} e+X^{++}(AI), \\ h\nu+X^{+}(DR). \end{cases} \tag{2}$$

The autoionizing state introduces a resonance in the cross section. Autoionization rate usually dominates DR when the outer electron is in a low to medium high n-level and DR dominates in the high n levels as n^3.

The unified method [15–17] considers the unified nature of the non-resonant and resonant parts of the (e + ion) recombination process and gives the total recombination rate. It also includes the radiation damping effect [18] using a scheme that fits the dipole matrix of the autoionizing resonance for autoionization and radiative decay rates and then extracts out radiative decay part from the S-matrix [19,20]. Unified method provides self-consistent set of atomic parameters for the inverse processes of photoionization and electron–ion recombination through using the *identical* coupled channel or close coupling (CC) wave function expansion for both the processes.

In the CC approximation, the wave function $\Psi(E)$ of the atomic system of the core (called the target) of N electrons and the interacting $(N+1)$th electron is expressed as

$$\Psi(E)=A\sum_i\chi_i\theta_i+\sum_j c_j\Phi_j, \tag{3}$$

χ_i represents the core or the target eigenfunction in a specific state $(S_iL_i)J_i\pi_i$, and θ_i is the interacting electron in a channel labeled as $S_iL_i(J_i)\pi_i k_i^2\ell_i(SL\pi$ or $J\pi))$; k_i^2 being its incident kinetic energy. The second term contains Φ_j's that represent the correlation functions of the $(N+1)$-electron system to account for short range correlation and the orthogonality between the continuum and the bound orbitals.

The relativistic Hamiltonian, in the Briet–Pauli R-matrix (BPRM) method developed under the Iron Project [9], is given by

$$H_{N+1}^{\rm BP}=H_{N+1}^{NR}+H_{N+1}^{\rm mass}+H_{N+1}^{\rm Dar}+H_{N+1}^{\rm so}, \tag{4}$$

where first term, H_{N+1}^{NR}, is the nonrelativistic Hamiltonian

$$H_{N+1}^{NR}=\sum_{i=1}^{N+1}\left\{-\nabla_i 2-\frac{2Z}{r_i}+\sum_{j>i}^{N+1}\frac{2}{r_{ij}}\right\}, \tag{5}$$

and the one-body relativistic correction terms are mass correction

$$H^{\rm mass}=-\frac{\alpha^2}{4}\sum_i p_i^4,$$

Darwin

$$H^{\rm Dar}=\frac{Z\alpha^2}{4}\sum_i\nabla^2\left(\frac{1}{r_i}\right)$$

and spin–orbit interaction

$$H^{\rm so}=Z\alpha^2\sum_i\frac{1}{r_i^3}\mathbf{l_i}\cdot\mathbf{s_i}.$$

While the first two improve the energies, the spin–orbit interaction splits the LS term into fine structure components. A part of two-body interaction terms is also included through couplings of channels. In BPRM method, the set of $SL\pi$ is recoupled for $J\pi$ levels of (e + ion)-system which is followed by diagonalization of the Hamiltonian, $H_{N+1}^{BP}\Psi=E\Psi$. The positive energy ($E=k^2\geq 0$) and negative energy ($E<0$) define the continuum Ψ_F or bound Ψ_B states which are used in the transition matrix elements.

The bound-free transition matrix is obtained from the reduced matrix element $\langle\Psi_B\|\mathbf{D}\|\Psi_F\rangle$ where $\mathbf{D}=\sum_i r_i$ is the dipole operator and the sum is the number of electrons. The dipole line strength, $\mathbf{S}=\left|\langle\Psi_B\|\mathbf{D}\|\Psi_F\rangle\right|^2$, gives the photoionization cross section

$$\sigma_{PI}=[4\pi^2/(3g_i c)]\omega\mathbf{S}, \tag{6}$$

where g_i is the statistical weight factor of the initial bound state. The radiation damping of the resonances is carried

out through the fitting procedure [18–20]. This is considered for resonances up to effective quantum number $v \le 10$ while resonances beyond $v > 10$ are treated with DR theory as discussed below.

The electron–ion recombination cross section σ_{RC} of levels up to $n \le 10$ is obtained from photoionization cross sections σ_{PI} using the principle of detailed balance as

$$\sigma_{\rm RC}(\epsilon) = \frac{\alpha^2}{4}\frac{g_i}{g_j}\frac{(\epsilon+I)^2}{\epsilon}\sigma_{\rm PI}, \tag{7}$$

where Rydberg unit has been used. α is the fine structure constant, ϵ is the photoelectron energy, g_j is the statistical weight factor of the recombined ion and I is the ionization potential. Under unified method, both RR and DR are being included in $\sigma_{\rm RC}$ since they correspond to both the background and resonances in σ_{PI}. Assuming the recombining ion in its ground state, the σ_{PI} corresponds to partial photoionization cross sections, leaving the ion in the ground state. The total recombination cross section, σ_{RC}, is the summed from contributions of all recombined levels. This sum also gives the location and strength of diagnostic dielectronic satellite (DES) lines in hot plasmas [21].

The recombination rate coefficient, $\alpha_R(nSLJ)$, of a recombined level $i{=}nSLJ$ is obtained by convolving the cross sections $\sigma_{RC}(i)$ over Maxwellian electron distribution $f(v,T)$ at a given temperature as

$$\alpha_R(i,T) = \int_0^\infty v f(v,T)\sigma_{RC}(i)\, dv, \tag{8}$$

where

$$f(v) = \frac{4}{\sqrt{\pi}}\left(\frac{m}{2kT}\right)^{3/2} v^2 e^{-mv^2/2kT}. \tag{9}$$

The sum of these individual rates $\sum_i \alpha_R(i,T)$ provides the contribution to the total recombination rate coefficient, α_R and the total recombination cross sections, $\sigma_{\rm RC}$.

Total electron–ion recombination corresponds to contributions from infinite number of recombined states. Unified method includes them from two groups: group (A) states $n \le n_o$ which provide the main contributions and group (B) states with $n_o < n \le \infty$, with $n_o \sim 10$. The recombination rate coefficients of group (A) states are obtained from the photoionization cross sections as described above. Group (B) levels, $n_{\rm o} < n \le \infty$, which are closely lying narrow resonances and dominated by DR, are treated through quantum defect theory of DR within the close coupling approximation [15,16,22]. The DR collision strengths, Ω(DR), of these states are obtained from

$$\Omega(DR) = \sum_{SLJ\pi}\sum_n (1/2)(2J+1)P_n^{SLJ\pi}(DR), \tag{10}$$

where the DR probability $P_n^{SLJ\pi}$ in entrance channel n is, $P_n^{SLJ\pi}({\rm DR}) = (1-\mathcal{S}^{\dagger}_{\boldsymbol{ee}}\mathcal{S}_{\boldsymbol{ee}})_n$, $\mathcal{S}_{\rm ee}$ is the matrix for electron scattering *including* radiation damping. The cross section, σ_{RC} in Mb, and collision strength, $\Omega_{\rm RC}$, for recombination are related as

$$\sigma_{RC}(i\to j)(Mb) = \frac{\pi}{g_i k_i^2}\Omega_{RC}(i,j)(a_o^2/10^{-18}), \tag{11}$$

where k_i^2 is in Rydberg. For numerical stability, Ω_{RC} is preferable to σ_{RC} for calculation of recombination rate coefficient since σ_{RC} diverges at zero-photoelectron energy. The background contribution of $n_{\rm o} < n \le \infty$ state is negligible except at very low temperature. These contributions, referred to as the "high-n top-up", are added in hydrogenic approximation [23].

The detailed features of both the total recombination cross sections and the recombination rates $\alpha_{RC}(E)$ with photoelectron energy E convolved with an energy band can be measured experimentally. The velocity (v) or energy dependent recombination rate can be obtained as

$$\alpha_{RC}(E) = v\sigma_{RC}(E). \tag{12}$$

The observed features in $\alpha_{RC}(E)$ convolved with monochromatic bandwidth of the experimental beam in synchrotron facilities such as the Test Storage Ring in Heidelberg have been reported (e.g. [13]).

Table 1
Radiative decay rates (A-values), for dipole allowed transitions from various excited level to the ground level $2s^22p^5(^2P^o_{3/2})$ of core Fe XVIII. Transition level numbers correspond to those listed in [14]. Only the first transition correspond to decay from $n{=}2$ level, the rest are from $n{=}3$ levels.

Levels	Transition	A (s^{-1})
1-3	$2s^22p^5(^2P^o_{3/2})-2s2p^6(^2S_{1/2})$	9.04(10)
1-4	$2s^22p^5(^2P^o_{3/2})-2s^22p^43s(^4P_{5/2})$	6.20(10)
1-5	$2s^22p^5(^2P^o_{3/2})-2s^22p^43s(^2P_{3/2})$	1.19(12)
1-6	$2s^22p^5(^2P^o_{3/2})-2s^22p^43s(^2P_{1/2})$	8.34(11)
1-7	$2s^22p^5(^2P^o_{3/2})-2s^22p^43s(^4P_{3/2})$	5.71(11)
1- 8	$2s^22p^5(^2P^o_{3/2})-2s^22p^43s(^4P_{1/2})$	8.10(10)
1-9	$2s^22p^5(^2P^o_{3/2})-2s^22p^43s(^2D_{5/2})$	6.31(11)
1-10	$2s^22p^5(^2P^o_{3/2})-2s^22p^43s(^2D_{3/2})$	1.07(10)
1-20	$2s^22p^5(^2P^o_{3/2})-2s^22p^43s(^2S_{1/2})$	1.67(11)
1-31	$2s^22p^5(^2P^o_{3/2})-2s^22p^43d(^4D_{5/2})$	6.23(6)
1-33	$2s^22p^5(^2P^o_{3/2})-2s^22p^43d(^4D_{3/2})$	4.71(9)
1- 34	$2s^22p^5(^2P^o_{3/2})-2s^22p^43d(^4D_{1/2})$	2.58(12)
1-37	$2s^22p^5(^2P^o_{3/2})-2s^22p^43d(^4P_{1/2})$	5.72(9)
1-39	$2s^22p^5(^2P^o_{3/2})-2s^22p^43d(^4P_{3/2})$	4.39(12)
1-41	$2s^22p^5(^2P^o_{3/2})-2s^22p^43d(^4P_{5/2})$	7.90(12)
1-42	$2s^22p^5(^2P^o_{3/2})-2s^22p^43d(^2P_{1/2})$	2.77(11)
1-43	$2s^22p^5(^2P^o_{3/2})-2s^22p^43d(^2D_{3/2})$	1.21(12)
1-44	$2s^22p^5(^2P^o_{3/2})-2s^22p^43d(^2F_{5/2})$	8.83(9)
1-46	$2s^22p^5(^2P^o_{3/2})-2s^22p^43d(^4F_{3/2})$	3.16(11)
1-47	$2s^22p^5(^2P^o_{3/2})-2s^22p^43d(^4P_{5/2})$	3.12(11)
1-48	$2s^22p^5(^2P^o_{3/2})-2s^22p^43d(^2P_{3/2})$	4.98(11)
1-49	$2s^22p^5(^2P^o_{3/2})-2s^22p^43d(^4F_{5/2})$	5.32(12)
1-52	$2s^22p^5(^2P^o_{3/2})-2s^22p^43d(^2F_{5/2})$	7.81(11)
1- 53	$2s^22p^5(^2P^o_{3/2})-2s^22p^43d(^2S_{1/2})$	1.15(13)
1-55	$2s^22p^5(^2P^o_{3/2})-2s^22p^43d(^2P_{3/2})$	1.34(13)
1-56	$2s^22p^5(^2P^o_{3/2})-2s^22p^43d(^2D_{5/2})$	1.18(13)
1-57	$2s^22p^5(^2P^o_{3/2})-2s^22p^43d(^2D_{3/2})$	2.40(12)
1-58	$2s^22p^5(^2P^o_{3/2})-2s^22p^43d(^2P_{1/2})$	2.87(12)
1-59	$2s^22p^5(^2P^o_{3/2})-2s^22p^43d(^2D_{5/2})$	1.27(12)
1- 60	$2s^22p^5(^2P^o_{3/2})-2s^22p^43d(^2D_{3/2})$	1.36(11)

3. Computations

A 60-CC wave function expansion for Fe XVII [5,14], where the levels go up to 3d levels, was used both for photoionization and recombination calculations. The details of the close-coupling wave function and calculations of photoionization cross sections were given in the earlier papers [5,14].

The level-specific recombination rate coefficients $\alpha_R(i)$ with $n \leq 10$ were obtained from code RECOMB [23] and are added together for the total. The DR collision strengths for the narrow and dense resonances in the energy region, $10 < \nu \leq \infty$, below each target excited threshold were obtained using STGFDR [16,18]. They are mainly below the thresholds that are allowed for dipole transitions of the core. The radiative decay rates or the A-values for the electric dipole allowed excited thresholds to the core ground levels used in calculations of $\Omega(DR)$ are given in Table 1. They were obtained using the later version of the atomic structure code SUPERSTRUCTURE [12]. The contributions from all $n \leq \infty$ were added for the total unified $\sigma_{RC}(E)$, $\alpha_R(E)$ and $\alpha_R(T)$ using programs RECXS [24] and PRCOMG [25].

4. Results and discussion

The following subsections present sample results for photoionization cross sections of levels that play dominant role to recombination and illustrative features of electron–ion recombination and recombination rates.

4.1. Photoionization

Recombination rates require the partial photoionization cross sections corresponding to the recombining state, typically the ground state, of the recombining ion. Since the recombination cross section σ_{RC} is proportional to that of photoionization, the recombination rate varies with the positions of the resonances and the background in σ_{PI}.

Fig. 1 presents partial photoionization cross sections of three levels of Fe XVII, the ground $2s^2 2p^6(^1S_0)$ level and two excited levels $2s^2 2p^5 3p(^3D_3)$ and $2s^2 2p^5 3d(^3F^o_4)$, leaving the core in the ground level. The low energy region of the ground level show that the $n=2$ resonances are stronger than those of $n=3$ core excitations (regions showed with arrows). However, for the excited levels, the channels with $n=2$ core levels are almost negligible

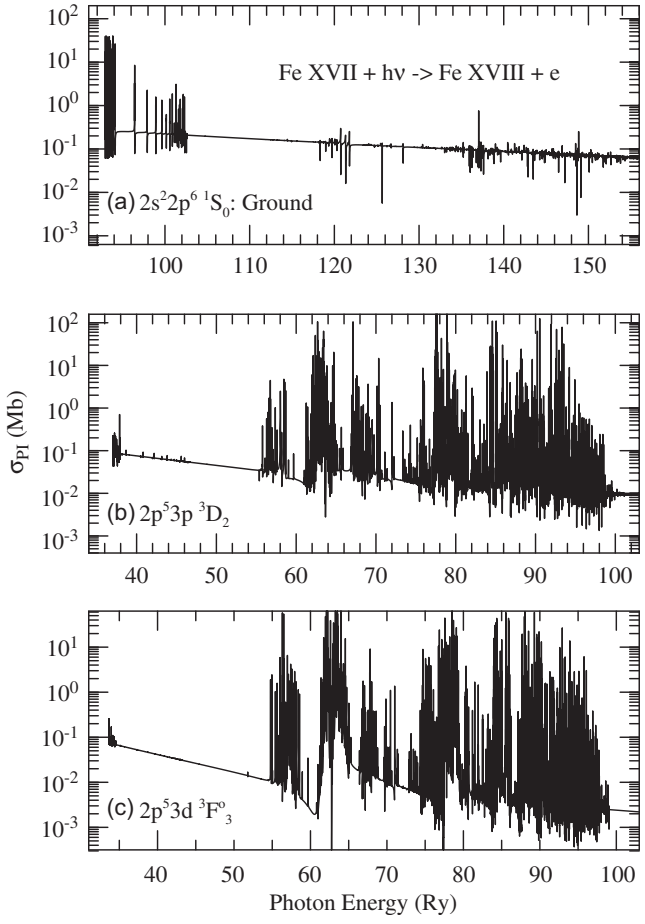

Fig. 1. Photoionization cross sections of the (a) ground $2s^2 2p^6(^1S_0)$ and two excited levels (b) $2s^2 2p^5 3p(^3D_3)$ and (c) $2s^2 2p^5 3d(^3F^o_4)$ of Fe XVII. These illustrate the strong couplings of channels with $n=2$ core levels for the ground state and with $n=3$ core levels for the excited levels. Arrows show energy range dominated by $n=2$ and $n=3$ core excitations.

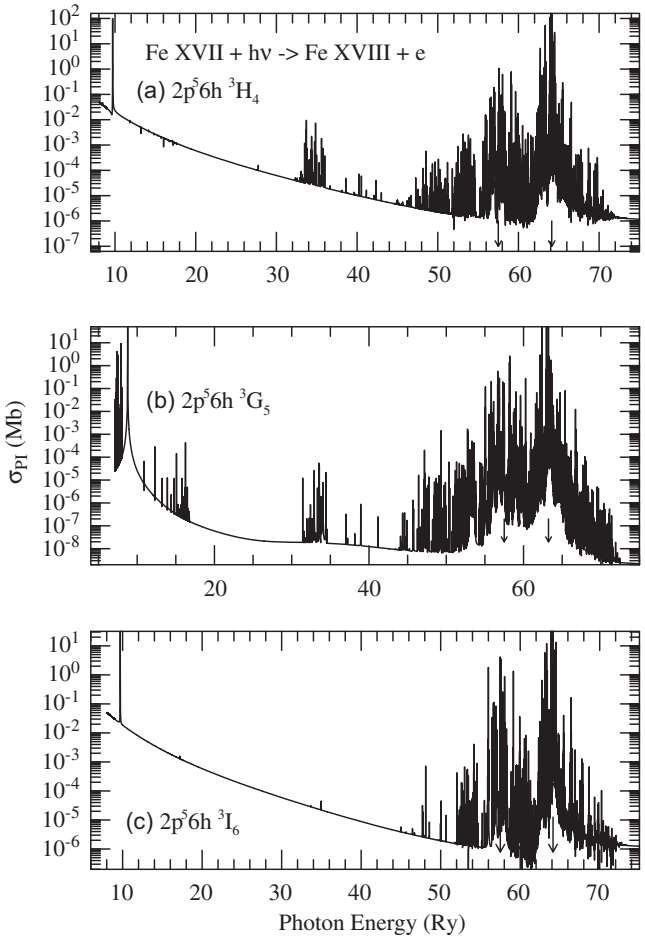

Fig. 2. Photoionization cross sections of three excited levels of Fe XVII: (a) $2p^5 6h(^3H_4)$, (b) $2p^5 6h(^3G_5)$, (c) $2p^5 6h(^3I_5)$ illustrating PEC resonances. The two arrows indicate energy positions of PEC resonances. However, the enhancement correspond to 29 PEC resonances (Table 1) in the energy regions. Due to these resonances, the levels contribute considerably to electron–ion recombination in the high temperature.

compared to those with $n=3$ core levels which introduce stronger and prominent resonances over a large energy range. The arrows in the figure cover energy ranges dominated by $n=2$ and $n=3$ core excitations. All these three levels have relatively high background cross sections in the low energy region and with higher energy they decay slowly particularly for the ground level. Hence these levels, especially the ground level, dominate the recombination in the low temperature ($<10^6$ K). The high peak resonances of the excited levels contribute significantly to recombination, but are also dampened by the $\exp(kT/E)$ factor in the recombination rate.

The recombination at high temperature region is usually dominated by excited levels which show large PEC (photoexcitation-of-core) or Seaton resonances in σ_{PI} in addition to narrow Rydberg resonances. Giant PEC [26,27] resonances appear in σ_{PI} of excited levels with a single valence electron and at photon frequencies corresponding to strong dipole transitions in the core, such as listed in Table 1. The table shows that there is only one dipole allowed transition from $n=2$ complex, and 28 from $n=3$ complex. A number of $n=3$ levels decaying to the ground level have rates about two orders of magnitude higher than that from $n=2$ level $2s2p^6(^2S_{1/2})$ indicating stronger resonances. The width and height of PEC resonances are typically orders of magnitude larger than those of individual Rydberg resonances. For Fe XVII, PEC resonances due to core transitions to $n=3$ levels are considerably huge as shown in Fig. 2. The figure presents σ_{PI} of three excited levels of Fe XVII, (a) $2p^56h(^3H_4)$, (b) $2p^56h(^3G_5)$, (c) $2p^56h(^3I_5)$. For this ion, the levels with $2p^56h$ are found to dominate the recombination.

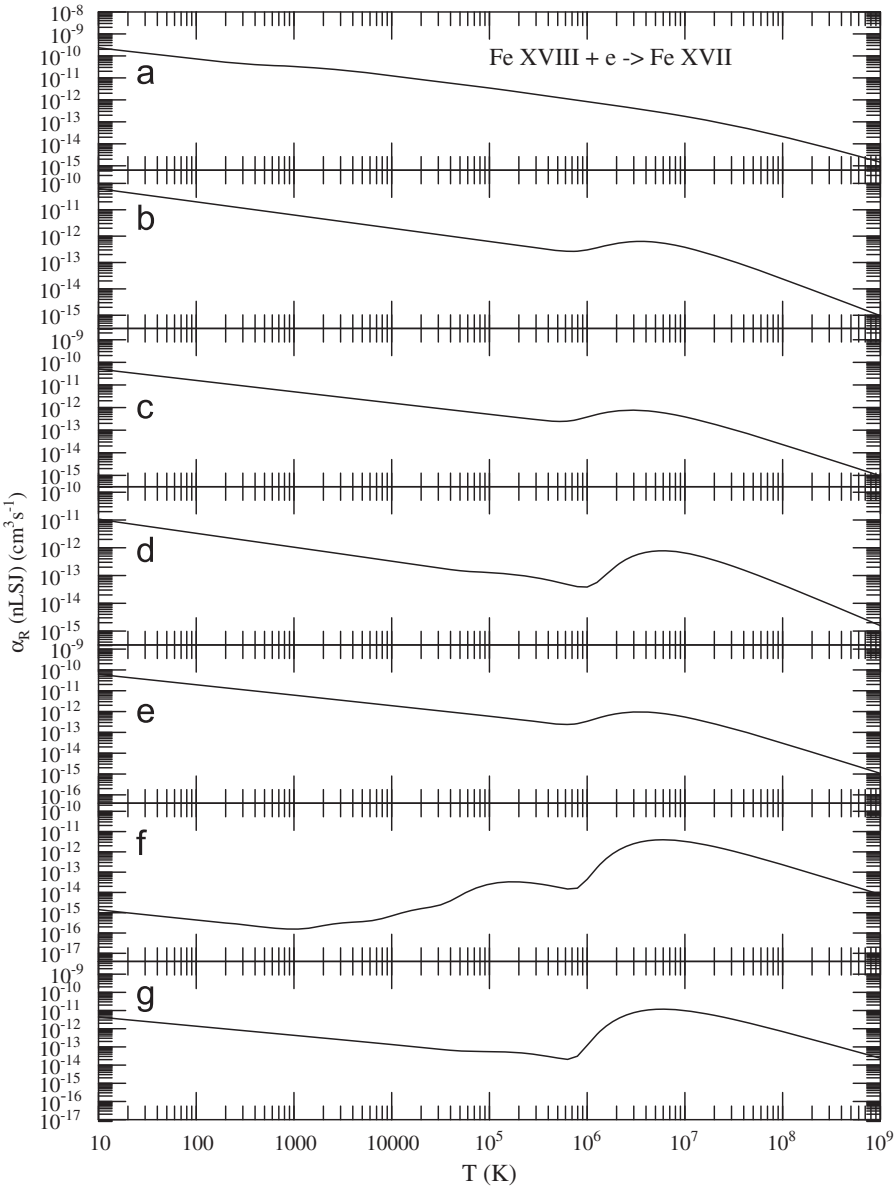

Fig. 3. Level-specific recombination rate coefficients, including both RR and DR, of the ground (a) and some excited levels (b–g) of Fe XVII. Except the ground level, excited levels show DR bumps whose positions and strengths depend on the resonant features in the photoionization cross sections. (a) $2s^22p^6(^1S)$: Ground, (b) $2p^53p(^3D_2)$, (c) $2p^53s(^3P^o2)$, (d) $2p^56f(^3G^o_3)$, (e) $2p^53d(^3F^o_3)$, (f) $2p^56h(^3G_5)$ and (g) $2p^55g(^3H^o_6)$.

Table 2
Level-specific recombination rate coefficients $\alpha_R(nSL\pi)$ of the ground and several dominant excited levels of Fe XVII. BE is the binding energy in Ry of the level.

$\mathrm{Log}_{10}T$	$\alpha_R(nSL\pi)$ (cm^3/s)						
BE(RY)=	$2s^22p^6(^1S_0)$ −9.29E+01	$2s^22p^53p(^3P_2)$ −3.67E+01	$2s^22p^53p(^3D_3)$ −3.69E+01	$2s^22p^56h(^3H_4)$ −8.03E+00	$2s^22p^53d(^3F_4^o)$ −3.37E+01	$2s^22p^56h(^3H_5)$ −7.09E+00	$2s^22p^56h(^3I_6)$ −8.03E+00
1.0	2.36E−10	6.51E−11	9.04E−11	3.02E−12	8.22E−11	1.43E−15	4.47E−12
1.1	2.07E−10	5.72E−11	7.94E−11	2.66E−12	7.22E−11	1.25E−15	3.92E−12
1.2	1.84E−10	5.06E−11	7.03E−11	2.35E−12	6.39E−11	1.11E−15	3.47E−12
1.3	1.63E−10	4.50E−11	6.25E−11	2.09E−12	5.68E−11	9.86E−16	3.09E−12
1.4	1.45E−10	4.01E−11	5.56E−11	1.86E−12	5.06E−11	8.78E−16	2.75E−12
1.5	1.29E−10	3.57E−11	4.96E−11	1.66E−12	4.51E−11	7.82E−16	2.45E−12
1.6	1.15E−10	3.18E−11	4.42E−11	1.48E−12	4.02E−11	6.97E−16	2.18E−12
1.7	1.03E−10	2.83E−11	3.93E−11	1.32E−12	3.58E−11	6.21E−16	1.94E−12
1.8	9.15E−11	2.53E−11	3.51E−11	1.17E−12	3.19E−11	5.53E−16	1.73E−12
1.9	8.16E−11	2.25E−11	3.13E−11	1.05E−12	2.84E−11	4.93E−16	1.54E−12
2.0	7.27E−11	2.01E−11	2.79E−11	9.32E−13	2.53E−11	4.40E−16	1.38E−12
2.1	6.48E−11	1.79E−11	2.48E−11	8.30E−13	2.26E−11	3.92E−16	1.23E−12
2.2	5.78E−11	1.59E−11	2.21E−11	7.40E−13	2.01E−11	3.49E−16	1.09E−12
2.3	5.17E−11	1.42E−11	1.97E−11	6.59E−13	1.79E−11	3.11E−16	9.74E−13
2.4	4.66E−11	1.27E−11	1.76E−11	5.88E−13	1.60E−11	2.78E−16	8.68E−13
2.5	4.28E−11	1.13E−11	1.57E−11	5.24E−13	1.42E−11	2.48E−16	7.74E−13
2.6	4.02E−11	1.01E−11	1.40E−11	4.67E−13	1.27E−11	2.21E−16	6.89E−13
2.7	3.84E−11	8.96E−12	1.24E−11	4.16E−13	1.13E−11	1.97E−16	6.14E−13
2.8	3.68E−11	7.99E−12	1.11E−11	3.71E−13	1.01E−11	1.76E−16	5.47E−13
2.9	3.51E−11	7.12E−12	9.88E−12	3.30E−13	8.99E−12	1.60E−16	4.88E−13
3.0	3.30E−11	6.35E−12	8.81E−12	2.94E−13	8.01E−12	1.53E−16	4.34E−13
3.1	3.08E−11	5.66E−12	7.85E−12	2.62E−13	7.14E−12	1.62E−16	3.87E−13
3.2	2.87E−11	5.04E−12	7.00E−12	2.33E−13	6.36E−12	1.90E−16	3.45E−13
3.3	2.66E−11	4.49E−12	6.24E−12	2.08E−13	5.67E−12	2.32E−16	3.07E−13
3.4	2.46E−11	4.00E−12	5.56E−12	1.85E−13	5.05E−12	2.78E−16	2.73E−13
3.5	2.25E−11	3.57E−12	4.95E−12	1.65E−13	4.50E−12	3.16E−16	2.43E−13
3.6	2.03E−11	3.18E−12	4.42E−12	1.46E−13	4.01E−12	3.42E−16	2.16E−13
3.7	1.82E−11	2.84E−12	3.93E−12	1.30E−13	3.57E−12	3.64E−16	1.93E−13
3.8	1.61E−11	2.53E−12	3.51E−12	1.16E−13	3.18E−12	4.09E−16	1.71E−13
3.9	1.42E−11	2.25E−12	3.13E−12	1.03E−13	2.84E−12	5.11E−16	1.52E−13
4.0	1.25E−11	2.01E−12	2.79E−12	9.13E−14	2.53E−12	7.01E−16	1.35E−13
4.1	1.10E−11	1.79E−12	2.48E−12	8.09E−14	2.25E−12	9.72E−16	1.20E−13
4.2	9.64E−12	1.59E−12	2.21E−12	7.16E−14	2.01E−12	1.29E−15	1.06E−13
4.3	8.45E−12	1.42E−12	1.97E−12	6.33E−14	1.79E−12	1.59E−15	9.38E−14
4.4	7.42E−12	1.27E−12	1.76E−12	5.59E−14	1.59E−12	1.90E−15	8.29E−14
4.5	6.52E−12	1.13E−12	1.57E−12	4.97E−14	1.41E−12	2.43E−15	7.33E−14
4.6	5.74E−12	1.01E−12	1.40E−12	4.54E−14	1.26E−12	3.81E−15	6.54E−14
4.7	5.06E−12	8.96E−13	1.24E−12	4.40E−14	1.12E−12	6.92E−15	5.99E−14
4.8	4.46E−12	7.99E−13	1.11E−12	4.61E−14	9.94E−13	1.22E−14	5.69E−14
4.9	3.93E−12	7.12E−13	9.88E−13	5.08E−14	8.83E−13	1.89E−14	5.59E−14
5.0	3.46E−12	6.34E−13	8.80E−13	5.60E−14	7.83E−13	2.57E−14	5.55E−14
5.1	3.02E−12	5.65E−13	7.84E−13	5.94E−14	6.94E−13	3.08E−14	5.44E−14
5.2	2.63E−12	5.04E−13	6.99E−13	5.99E−14	6.14E−13	3.32E−14	5.18E−14
5.3	2.28E−12	4.49E−13	6.23E−13	5.71E−14	5.42E−13	3.30E−14	4.76E−14
5.4	1.98E−12	4.00E−13	5.54E−13	5.17E−14	4.77E−13	3.05E−14	4.22E−14
5.5	1.71E−12	3.56E−13	4.94E−13	4.49E−14	4.19E−13	2.68E−14	3.61E−14
5.6	1.48E−12	3.19E−13	4.41E−13	3.76E−14	3.68E−13	2.25E−14	3.00E−14
5.7	1.28E−12	2.93E−13	4.01E−13	3.06E−14	3.27E−13	1.82E−14	2.44E−14
5.8	1.11E−12	2.93E−13	3.84E−13	2.49E−14	3.12E−13	1.48E−14	2.06E−14
5.9	9.60E−13	3.38E−13	4.04E−13	2.70E−14	3.48E−13	1.62E−14	3.09E−14
6.0	8.32E−13	4.39E−13	4.70E−13	7.19E−14	4.61E−13	4.45E−14	1.22E−13
6.1	7.20E−13	5.86E−13	5.79E−13	2.63E−13	6.52E−13	1.64E−13	4.89E−13
6.2	6.24E−13	7.48E−13	7.13E−13	7.67E−13	8.89E−13	4.80E−13	1.45E−12
6.3	5.39E−13	8.87E−13	8.42E−13	1.70E−12	1.12E−12	1.06E−12	3.21E−12
6.4	4.66E−13	9.73E−13	9.38E−13	3.00E−12	1.29E−12	1.87E−12	5.66E−12
6.5	4.01E−13	9.95E−13	9.80E−13	4.38E−12	1.38E−12	2.73E−12	8.26E−12
6.6	3.44E−13	9.55E−13	9.64E−13	5.52E−12	1.36E−12	3.44E−12	1.04E−11
6.7	2.94E−13	8.69E−13	8.97E−13	6.17E−12	1.27E−12	3.85E−12	1.16E−11
6.8	2.50E−13	7.57E−13	7.97E−13	6.28E−12	1.13E−12	3.92E−12	1.18E−11
6.9	2.11E−13	6.34E−13	6.80E−13	5.94E−12	9.60E−13	3.70E−12	1.12E−11
7.0	1.78E−13	5.16E−13	5.61E−13	5.29E−12	7.88E−13	3.30E−12	9.93E−12
7.1	1.48E−13	4.10E−13	4.51E−13	4.49E−12	6.29E−13	2.80E−12	8.43E−12
7.2	1.23E−13	3.19E−13	3.54E−13	3.68E−12	4.91E−13	2.29E−12	6.89E−12
7.3	1.01E−13	2.44E−13	2.74E−13	2.92E−12	3.76E−13	1.82E−12	5.47E−12
7.4	8.26E−14	1.84E−13	2.08E−13	2.26E−12	2.84E−13	1.41E−12	4.25E−12

Table 2 (*continued*)

$\text{Log}_{10}T$	$\alpha_R(nSL\pi)$ (cm^3/s)						
BE(RY)=	$2s^22p^6(^1S_0)$ −9.29E+01	$2s^22p^53p(^3P_2)$ −3.67E+01	$2s^22p^53p(^3D_3)$ −3.69E+01	$2s^22p^56h(^3H_4)$ −8.03E+00	$2s^22p^53d(^3F_4^o)$ −3.37E+01	$2s^22p^56h(^3H_5)$ −7.09E+00	$2s^22p^56h(^3I_6)$ −8.03E+00
7.5	6.70E−14	1.38E−13	1.57E−13	1.72E−12	2.11E−13	1.07E−12	3.23E−12
7.6	5.40E−14	1.02E−13	1.17E−13	1.29E−12	1.56E−13	8.05E−13	2.42E−12
7.7	4.32E−14	7.53E−14	8.67E−14	9.58E−13	1.14E−13	5.97E−13	1.80E−12
7.8	3.44E−14	5.53E−14	6.39E−14	7.03E−13	8.33E−14	4.38E−13	1.32E−12
7.9	2.71E−14	4.04E−14	4.69E−14	5.13E−13	6.04E−14	3.19E−13	9.60E−13
8.0	2.13E−14	2.94E−14	3.43E−14	3.71E−13	4.36E−14	2.31E−13	6.96E−13
8.1	1.66E−14	2.13E−14	2.50E−14	2.68E−13	3.14E−14	1.67E−13	5.01E−13
8.2	1.29E−14	1.55E−14	1.82E−14	1.92E−13	2.25E−14	1.20E−13	3.60E−13
8.3	9.98E−15	1.12E−14	1.32E−14	1.38E−13	1.62E−14	8.57E−14	2.58E−13
8.4	7.67E−15	8.09E−15	9.57E−15	9.84E−14	1.16E−14	6.13E−14	1.84E−13
8.5	5.87E−15	5.84E−15	6.93E−15	7.01E−14	8.27E−15	4.37E−14	1.31E−13
8.6	4.48E−15	4.21E−15	5.01E−15	4.99E−14	5.91E−15	3.11E−14	9.36E−14
8.7	3.40E−15	3.04E−15	3.62E−15	3.55E−14	4.21E−15	2.21E−14	6.65E−14
8.8	2.57E−15	2.19E−15	2.62E−15	2.52E−14	3.01E−15	1.57E−14	4.73E−14
8.9	1.94E−15	1.58E−15	1.89E−15	1.79E−14	2.14E−15	1.12E−14	3.36E−14
9.0	1.46E−15	1.13E−15	1.36E−15	1.27E−14	1.53E−15	7.92E−15	2.38E−14

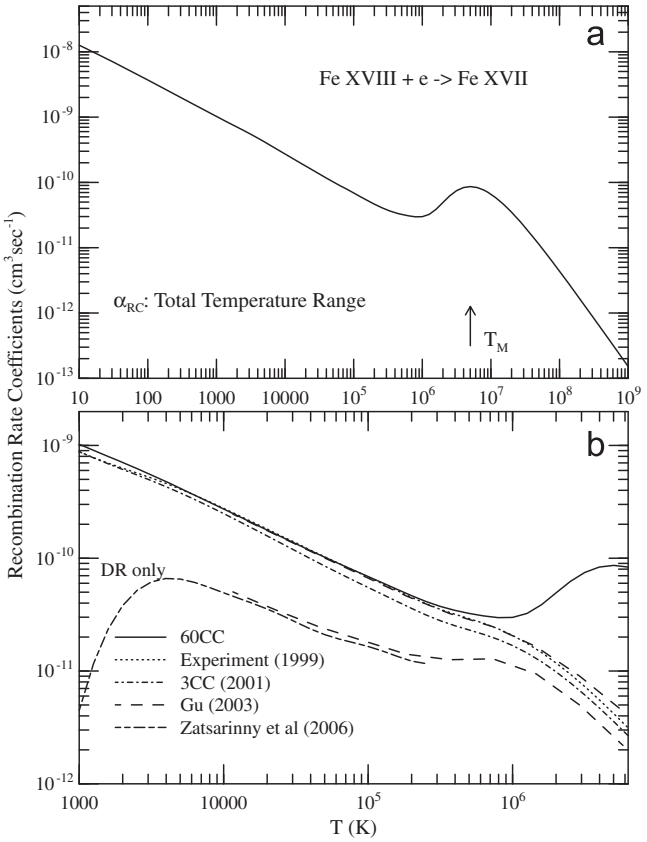

Fig. 4. (a) Total recombination rate coefficients of Fe XVII from 60CC (solid), (b) compared with those from 3CC (dot-dash [13]) calculations, by Gu (dash [6]), and those derived from experiment (dot [8]). The DR rates by Gu and by Zatsarinny et al. (short and long dash [7]) are also given to show the good agreement between the two indicating the total can have the similar agreement. Total α_{RC} from all four sources is about the same at low T until $\sim 10^6$ K where high-T DR starts to deviate and forms a DR peak at $T_M = 5 \times 10^6$ K, indicating dominant recombination at high temperature.

4.2. Electron–ion recombination

One important part of Fe XVII recombination is the features in very high temperature region. It was noticed from atomic structure calculations that the radiative decay rates (A-values) for $n=3$ terms are a few orders of magnitude higher than those of $n=2$ terms (Table 1) indicating the strong dipole transitions effect in photoionization and electron–ion recombination, similar to the case of Fe XXI [28,29]. Strong radiative decay rates indicate dominance of the resonant dielectronic recombination.

The present work reports level-specific recombination rate coefficients $\alpha_{RC}(j\pi)$ of all 454 levels with $n \le 10$. These rate coefficients include both the RR and DR contributions and hence represent the total rates for the level. Except the ground level, excited levels exhibit one or multiple DR peaks as seen in Fig. 3. The figure presents $\alpha_{RC}(LSJ\pi)$ of ground and some excited levels illustrating the features with DR bumps. The locations and strengths of the DR peak depend on those of the resonances in photoionization cross sections.

Table 2 presents level-specific rate coefficients of the ground and six other excited levels that dominant the total recombination in low and in high temperature regions. Level specific rates are needed in determination of the populations of levels.

The total recombination rate coefficient for Fe XVII is shown in Fig. 4. The solid curve represents $\alpha_{RC}(T)$ from the present 60-CC calculations. The present $\alpha_{RC}(T)$ is compared in Fig. 4(b) with the earlier rates from three CC BPRM calculations (dot-dash [13]), those by Gu (dash, the RR and DR rates have been summed for the total [6]). and those derived from experiment (dot [8]). The DR rates by Zatsarinny et al. [7] and by Gu [6] are also presented to show that both calculations would give similar total rates when RR is added to DR by Zatsarinny et al. These earlier studies correspond to low temperature region. Very good agreement of recombination rates can be found in the low temperature region for all five, the 60CC, the 3 CC, those by Gu, by Zatsarinnuy et al. and the results derived from experiment. The small difference of about 20% between the experimentally derived and 3CC rate coefficients is seen to have improved with 60CC calculations where they merge in the low temperature region. However, the

agreement deviates considerably as high temperature region is approached. The present calculations show that the total rate increases until at about $T_M = 5 \times 10^6$ K where the high energy resonant structures introduce a DR peak. Hence the existing recombination rate coefficients are underestimated considerably at high temperature. The numerical values of total $\alpha_{RC}(T)$ is tabulated in Table 3.

As mentioned above that the resonances in the recombination cross sections are observed as the dielectronic

Table 3
Total recombination rate coefficients, $\alpha_R(T)$ for (e + Fe XVIII → Fe XVII).

Log T	α_R	Log T	α_R
1.00	1.263E−08		
1.10	1.122E−08		
1.20	9.952E−09		
1.30	8.821E−09		
1.40	7.819E−09		
1.50	6.922E−09		
1.60	6.116E−09		
1.70	5.404E−09		
1.80	4.774E−09		
1.90	4.206E−09		
2.00	3.705E−09		
2.10	3.265E−09		
2.20	2.870E−09		
2.30	2.520E−09		
2.40	2.215E−09		
2.50	1.945E−09		
2.60	1.709E−09		
2.70	1.503E−09		
2.80	1.321E−09		
2.90	1.162E−09		
3.00	1.024E−09		
3.10	9.041E−10		
3.20	7.985E−10		
3.30	7.055E−10		
3.40	6.222E−10		
3.50	5.470E−10		
3.60	4.788E−10		
3.70	4.176E−10		
3.80	3.633E−10		
3.90	3.149E−10		
4.00	2.729E−10		
4.10	2.364E−10		
4.20	2.049E−10		
4.30	1.778E−10		
4.40	1.545E−10		
4.50	1.344E−10		
4.60	1.169E−10		
4.70	1.020E−10		
4.80	8.931E−11		
4.90	7.833E−11		
5.00	6.884E−11		
5.10	6.046E−11		
5.20	5.304E−11		
5.30	4.662E−11		
5.40	4.137E−11		
5.50	3.738E−11		
5.60	3.451E−11		
5.70	3.240E−11		
5.80	3.080E−11		
5.90	2.974E−11		
6.00	2.988E−11		
6.10	3.240E−11		
6.20	3.870E−11		
6.30	4.920E−11		
6.40	6.231E−11		
6.50	7.483E−11		
6.60	8.349E−11		
6.70	8.639E−11		
6.80	8.349E−11		
6.90	7.609E−11		
7.00	6.605E−11		
7.10	5.508E−11		
7.20	4.447E−11		
7.30	3.498E−11		
7.40	2.694E−11		
7.50	2.041E−11		
7.60	1.525E−11		
7.70	1.128E−11		
7.80	8.270E−12		
7.90	6.023E−12		
8.00	4.364E−12		
8.10	3.148E−12		
8.20	2.263E−12		
8.30	1.623E−12		
8.40	1.161E−12		
8.50	8.295E−13		
8.60	5.918E−13		
8.70	4.217E−13		
8.80	3.003E−13		
8.90	2.137E−13		
9.00	1.520E−13		

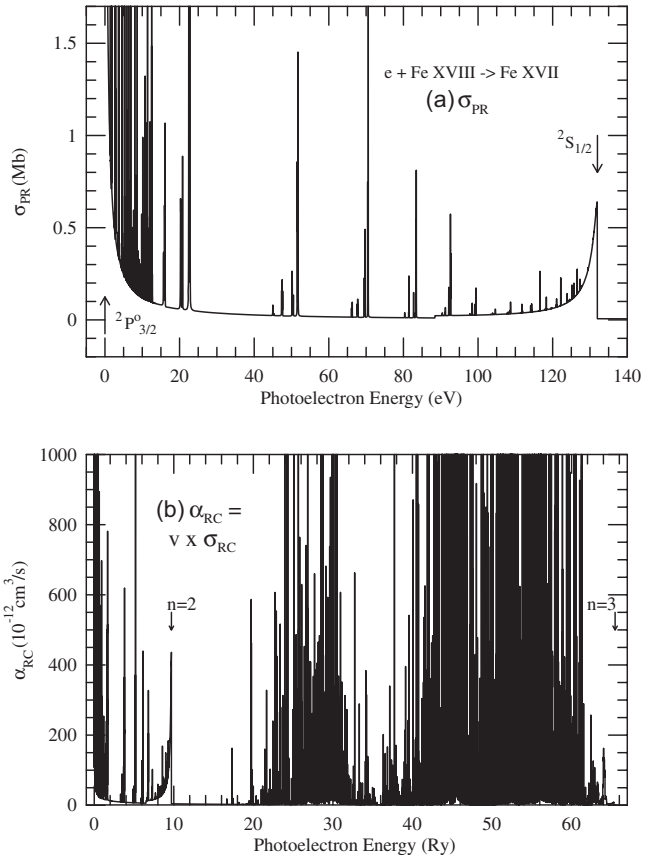

Fig. 5. (a) Total recombination cross sections σ_{RC} and (b) total rate coefficients α_{RC}(E) with respect to photoelectron energy. The arrows indicate the energy limits for $n=2$ and $n=3$ core excitations. (a) σ_{PR} and (b) $\sigma_{PR}=v \times \sigma_{PR}$.

satellite (DES) lines [21]. Fig. 5 presents (a) total recombination cross sections σ_{RC} in the low energy region and (b) total rate coefficients α_{RC}(E) with respect to photoelectron energy. These low energy resonant or DES lines are usually used for diagnostics lines. Fig. 5(a) shows that the background recombination cross section decreases with energy. As the energy approaches to $2s2p^6(^2S_{1/2})$ threshold of core ion Fe XVIII, the background cross section rises to a peak at the threshold beyond which it drops to zero. It is due to excitation of core to $2s2p^6(^2S_{1/2})$ from the ground level $2s^22p^5(^2P^o_{3/2})$ through electric dipole allowed transition. As the level $^2S_{1/2}$ is excited, electron flux trapped through DR below the threshold is released causing recombination cross section to go to zero. Earlier study [8,13] remained confined to this low energy region. The lower panel, Fig. 5(b), presents α_{RC}(E) for the entire energy range which exhibits strong recombination in the high energy regions due to $n=3$ core excitations. The recombination exceeds far from that due to $n=2$ core excitations.

As demonstrated in this work, the high energy recombination cross sections due to excitations to the $n=3$ levels are much larger and are more important. The rates peak at high temperatures close to the temperature, $T=4-5\times10^6$ K, of maximum abundance of Fe XVII in collisional equilibrium. The $\alpha_R(T)$ peaks at a temperature T_M of about 5×10^6 K corresponding to resonances converging on to the series limits of strong dipole $\Delta n=1$ transitions.

5. Conclusion

The detailed high temperature features in electron–ion recombination of the astrophysically important ion, Fe XVII, are presented for the first time. A broad DR bump due to strong high-peak resonances belonging to high energy core excitations to $n=3$ is found at temperature 5×10^6 K, where the ion has maximum abundance in high temperature plasma at coronal equilibrium. PEC and high-peak resonances in photoionization cross sections relevant to the peak are illustrated. These results indicate importance of couplings of channels with highly excited cores that are often ignored. The recombination rate coefficients at low temperature agree very well with the earlier experimental and theoretical rates. The results over a wide energy range for the electron–ion recombination and photoionization are obtained from extensive relativistic close coupling calculations. The presented results for the inverse processes are self-consistent by the unified method. Based on the agreement, consideration of relativistic effects, and the method, these results are expected to be accurate within 20%.

All data for photoionization and electron–ion recombination will be available at the NORAD-Atomic-Data [30] website.

Acknowledgments

This work was partially supported by the DOE and NSF. The computational work was carried out on Cray machines at the Ohio Supercomputer Center in Columbus, Ohio.

References

[1] Arnaud M, Raymond J. Iron ionization and recombination rates and ionization equilibrium. ApJ 1992;398:394–406.
[2] Laming JK, et al. Emission-line intensity ratios in Fe XVII observed with a microcalorimeter on an electron beam ion trap. ApJ 2000;545:L161–4.
[3] Mohan N, Le Dourneuf N, Hibbert A, Burke PG. Relativistic calculation for photoionization of the ground state of neonlike Fe XVII. Phys Rev A 1998;57:3489–92.
[4] Bhatia AK, Kastner SD. The optically thick Fe XVII spectrum: X-ray, extreme-ultraviolet, and forbidden line ratios. ApJ 1993;516:482–9.
[5] Zhang HL, Nahar SN, Pradhan AK. Relativistic close coupling calculations for photoionization and recombination of Ne-like Fe XVII. Phys Rev A 2001;64 032719-1-12.
[6] Gu MF. Recombination x-ray line formation of iron L-shell ions in low temperature plasmas. Astrophys J 2003;593:1249–54.
[7] Zatsarinny O, Gorczyca TW, Fu J, Korista KT, Badnell NR, Savin DW. Dielectronic recombination data for dynamic finite-density sequence. A & A 2006;447:379–87.
[8] Savin DW, et al. Dielectronic recombination in photoionized gas. II. Laboratory measurements for Fe XVIII and Fe XIX. ApJ Suppl Ser 1999;123:687–702.
[9] Hummer DG, Berrington KA, Eissner W, Pradhan AK, Saraph HE, Tully JA. Atomic data from the IRON project. 1: goals and methods. Astron Astrophys 1993;279:298–309.
[10] Berrington KA, Eissner W, Norrington PH. RMATRIX1: Belfast atomic R-matrix codes. Comput Phys Commun 1992;92:290–420.
[11] Chen GX, Pradhan AK, Eissner W. Breit–Pauli R-matrix calculations for electron impact excitation of Fe XVII: a benchmark study. J Phys B 2003;36:453–77.
[12] Nahar SN, Eissner W, Chen GX, Pradhan AK. Atomic data from the iron project. LIII. Relativistic allowed and forbidden transition probabilities for Fe XVII. A & A 2003;408:789–801.
[13] Pradhan AK, Nahar SN, Zhang H. Unified electronic recombination of Ne-like Fe XVII: implications for modeling X-ray plasmas. Astrophys J Lett 2001;549:L265–8.
[14] Nahar SN, Pradhan AK, Chen GX, Eissner W. Highly excited core resonances in photoionization of Fe xvii: implications for plasma opacities. Phys Rev A 2011;83 053417-1-12.
[15] Nahar SN, Pradhan AK. Electron–ion recombination in the close-coupling approximation. Phys Rev A 1992;45:7887–93.
[16] Nahar SN, Pradhan AK. Unified treatment of electron–ion recombination in the close-coupling approximation. Phys Rev A 1994;49:1816–35.
[17] Nahar SN, Pradhan AK. Unified electron–ion recombination rate coefficients of silicon and sulfur ions. ApJ 1995;447:966–79.
[18] Zhang HL, Nahar SN, Pradhan AK. Close coupling R-matrix calculations for electron–ion recombination cross sections. J Phys B 1999;32:1459–79.
[19] Sakimoto K, Terao M, Berrington KA. Effects of radiative decay on the bound-continuum transition of highly charged atomic ions. Phys Rev A 1990;42:291–5.
[20] Pradhan AK, Zhang HL. Radiation damping of autoionizing resonances. J Phys B 1997;30:L571–9.
[21] Nahar SN, Pradhan AK. Di-electronic satellite spectra of helium-like iron and nickel from the unified recombination method. Phys Rev A 2006;73 [062718-1-8].
[22] Bell RH, Seaton MJ. Dielectronic recombination: I. General theory. J Phys B 1985;18:1589–629.
[23] Nahar SN. Total electron–ion recombination of Fe iii. Phys Rev A 1996;53:2417–24.
[24] Nahar SN, Pradhan AK, Zhang H. Electron–ion recombination rate coefficients and photoionization cross sections for astrophysically abundant elements IV. Relativistic calculations for C IV and C V for UV and X-ray modeling. ApJ 2000;131:375–89.
[25] Nahar SN. Electron–ion recombination of Fe II. Phys Rev A 1997;55:1980–7.
[26] Yu Y, Seaton MJ. Atomic data for opacity calculations. IV. Photoionisation cross sections for C II. J Phys B 1987;20:6409–29.
[27] Nahar SN, Pradhan AK. Photoionization and electron–ion recombination: the carbon sequence. Phys Rev A 1991;44:2935–48.
[28] Nahar SN. Photoionization cross sections of Fe XXI. J Quant Spectrosc Radiat Transfer 2008;109:2417–26.
[29] Nahar SN. Electron–ion recombination and photoionization of Fe XXI. J Quant Spectrosc Radiat Transfer 2008;109:2731–42.
[30] NORAD website: 〈www.astronomy.ohio-state.edu/nahar/nahar_radiativeatomicdata〉.